



A micropillar array for sample concentration via in-plane evaporation

Jae-Woo Choi,^{1,a)} Seyyed Mohammad Hosseini Hashemi,^{1,b)}

David Erickson,^{2,c)} and Demetri Psaltis^{1,d)}

¹*School of Engineering, École Polytechnique Fédérale de Lausanne, Lausanne 1015, Switzerland*

²*Sibley School of Mechanical and Aerospace Engineering, Cornell University, Ithaca, New York 14853, USA*

(Received 5 May 2014; accepted 10 July 2014; published online 21 July 2014)

We present a method to perform sample concentration within a lab-on-a-chip using a microfluidic structure which controls the liquid-gas interface through a micropillar array fabricated in polydimethylsiloxane between microfluidic channels. The microstructure confines the liquid flow and a thermal gradient is used to drive evaporation at the liquid-gas-interface. The evaporation occurs in-plane to the microfluidic device, allowing for precise control of the ambient environment. This method is demonstrated with a sample containing 1 μm , 100 nm fluorescent beads and SYTO-9 labelled *Escherichia coli* bacteria. Over 100 s, the fluorescent beads and bacteria are concentrated by a factor of 10. © 2014 AIP Publishing LLC.

[<http://dx.doi.org/10.1063/1.4890943>]

INTRODUCTION

Sample concentration is a critical operation ubiquitous in lab-on-a-chip application due to the small volume of fluids and small concentration of samples.¹ A variety of methods to concentrate samples have been developed using pressure driven flow via syringe pumps,² electrophoresis,³ dielectrophoretic,⁴ centrifugal forces,⁵ magnetophoresis,⁶ optoelectronic,⁷ capillary flow,⁸ ion concentration polarization,⁹ and evaporation-induced flow.¹⁰ For evaporation-induced sample concentration, the fluidic flow is generally constant and the technique is applicable to any biological or chemical samples.¹⁰ In this paper, we focus on sample concentration via evaporation using a polydimethylsiloxane (PDMS) micropillar array adopting a technique developed for silicon microfluidic channels.¹¹ We apply this technique to aqueous samples containing bacteria and fluorescent agents.

Membrane-based liquid-gas separation is a well studied topic and has been reviewed extensively.^{12–15} These separations are used for adsorption, where gaseous phase is introduced into the liquids; stripping, where volatile components are removed from the liquid phase into the gas phase; and distillation, where miscible fluid mixtures are separated through vapour pressure and/or thermal differences. In this article, we focus on sample concentration as it applies to the lab-on-a-chip community where the samples are aqueous and the liquid flow is continuous.

Evaporation based microfluidic methods have been previously developed to perform sample concentration.^{16–27} These methods rely on controlling the evaporation at the outlet, replacing the vaporized liquid via capillary effects, and sucking liquid through the microfluidic channel at pre-determined rates.¹⁶ This evaporation rate can be actively controlled using pressure¹⁷ or temperature.¹⁸ It can be used to manipulate blood,¹⁹ bacteria,²⁰ DNA,²¹ and viruses²² or generate

^{a)}jae-woo.choi@epfl.ch

^{b)}mohammad.hashemi@epfl.ch

^{c)}de54@cornell.edu

^{d)}Author to whom correspondence should be addressed. Electronic mail: demetri.psaltis@epfl.ch. Tel.: +41 21 69-37798. Fax: +41 21 69-36930.

chemical gradients to perform chemotaxis experiments.²³ Additionally, structures within microfluidic channels,²⁴ open surface microchannel grooves,²⁵ open-surface micro-traps,²⁶ and super-hydrophobic nano-structures²⁷ can be used to concentrate compounds at selective locations. Most of these methods rely on evaporation into an ambient atmosphere at the outlet of the microfluidic channel. Concentrating compounds via structures within microfluidic channels²⁴ can be highly advantageous, since the fluids inside the channels can be rapidly modified.

Since evaporation is proportional to the surface area and also to the difference between the saturation and actual water vapour pressures near the surface of the liquid, we maintain a low water vapour pressure by having a thermal gradient between the water surface and the area where condensation takes place. In previous demonstrations, evaporation takes place from a large droplet at the outlet of the microfluidic channel, with a heat sink placed at some distance away from the chip. Miniaturizing this system, such that evaporation occurs inside the microfluidic channel, can result in a dramatic decrease of the total vaporized rate if the total area remains about the same without changing the thermal gradient.²⁸ Therefore, a goal of the microfluidic method is to increase both the: (1) surface area to volume ratio and (2) vapour pressure differentials via thermal gradients. These two components are an accepted advantage of microfluidics over traditional methods in energy applications,²⁹ chemical synthesis,³⁰ micro-reactors,³¹ biosensors,³² and medical diagnostics.³³

The issue of generating a microstructure to separate liquid and gaseous phase within microfluidics is tackled by a variety of debubbling mechanisms. Unwanted gas bubbles in microfluidic channels can be removed from continuous flow by open microfluidics³⁴ and various microstructures such as hydrophobic venting holes,³⁵ pneumatic bubble traps,³⁶ integrated bubble traps,³⁷ membrane based debubblers,³⁸ electrochemical debubblers,³⁹ and in-plane debubblers.⁴⁰

Improved performance is obtained via external pressure and thermal integration.⁴¹ Alternatively, these bubbles can be used as a means to valve fluidic flow.⁴² We were inspired by micropillar liquid-gas separations,¹¹ hydrophobic venting holes, and microfluidic debubblers to design a polymer-based microfluidic structure with micropillars, as shown in Figure 1.

DESIGN OPTIMIZATION

The microfluidic chip was made using PDMS (Sylgard). PDMS was mixed at a ratio of 10:1 base and curing agent. This was poured onto a SU-8 mold for the PDMS fluidics layer, made using photolithography on a Si wafer. A flat PDMS layer was made using an empty Si wafer. After punching inlet and outlet ports into the PDMS fluidics layers, the two pieces of PDMS are brought together. It has an inlet sample microfluidic channel with a width of 800 μm . There are 100 $\mu\text{m} \times 100 \mu\text{m}$ openings in between posts of 100 $\mu\text{m} \times 100 \mu\text{m}$ (width and length). These posts form a part of the liquid repellent structure, which separates liquid water from vapor water. The air cavity is 500 μm wide. The total structure is approximately 2800 μm wide. The two microfluidic channels are driven by gravity pressure from water tanks.

First, we simulate the microfluidic chip containing the liquid repellent structure in COMSOL to optimize parameters. A 3-dimensional version of the chip as shown in Figure 1 is modelled in COMSOL. Fluid flows into the sample microfluidic channel. The sample is heated to 30°C. The fluid velocity in the sample microfluidic channel is dependent on the amount of vaporized water. The amount of vaporized water is determined by the difference of the saturated vapour pressure and the actual vapour pressure near the hot body of water. Proportional to this difference, heat in the form of the enthalpy of vaporization is removed from the sample-liquid repellent structure interface. When a heat sink condenses the water vapour, the vapour pressure decreases, heat is released in the form of enthalpy of condensation, and additional evaporation from the hot body of water can occur. To model the amount of water which is evaporating from the sample interface and condensing on the air cavity, we use the mass transfer equation as described by Plesset.⁴³ Two bodies of water at different temperatures will have a mass flow of water which vaporizes from the hot body of water and condenses on the cold body of water, assuming salinity is equivalent. The equation is

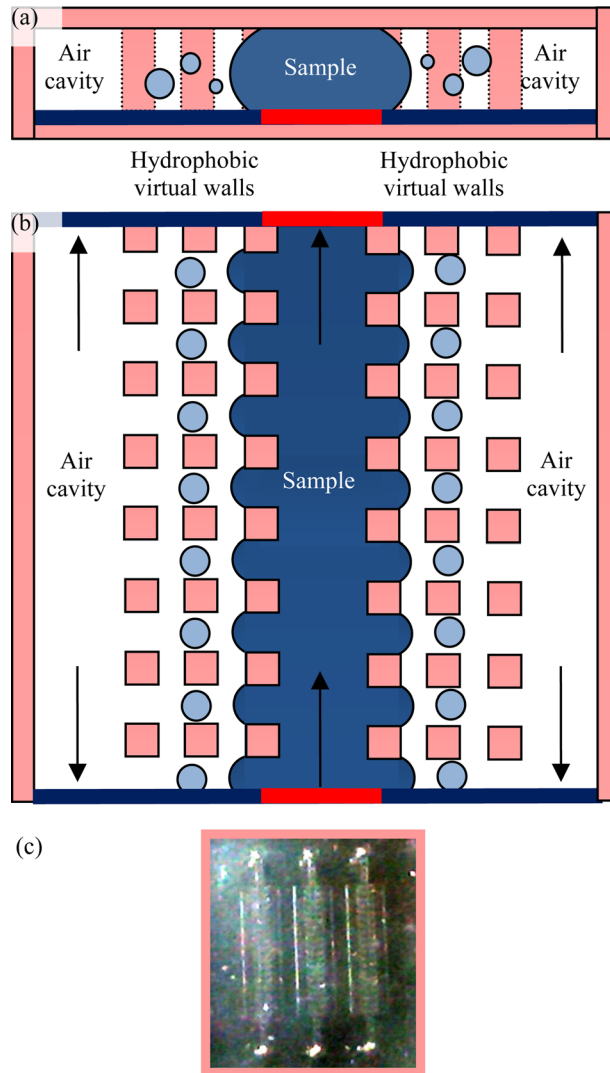


FIG. 1. (a) and (b) Side-view and top-down diagrams of liquid repellent structure. In the microfluidic chip, there is flowing sample which contains bacteria, particles, and chemicals to be concentrated. The liquid repellent structure, between the sample channel and the air cavity, allows water vapor through but not liquid water. The air cavity fills up with vapor. The vapor can condense in the cavity or escapes to the outlet ports. (c) A picture of a 1 cm \times 1 cm device, on a black background, with 3 parallel structures is shown.

$$J = \alpha \rho_0^e \sqrt{\frac{RT_0}{2\pi M}} \frac{1 - (\rho_1^e / \rho_0^e)(T_1 / T_0)}{1 + \sqrt{T_1 / T_0}},$$

where J is the mass flow rate, α is the evaporation coefficient, M is the molecular mass of the water, T_0 is the temperature at warmer interface, T_1 is the temperature at cooler interface, ρ_i^e is the saturation vapor density at T_i (i is either 0 or 1), and R is the universal gas constant.

In the simulations, we take the temperature along the sidewall of the sample microfluidic channel and the sidewall of the air cavity. After averaging in height, we take the temperature and plug into the equation for a differential length-scale of 0.1–1 μm , which is the smallest size of the simulation mesh. This energy is removed from the sample microfluidic channel and added to the sidewall of the air cavity. At steady-state, we sum up the total amount of water added per second in the air cavity. This is the amount of clean water generated or distillate output.

There are four parameters of the microfluidic chip which are varied in the simulation: microfluidic cavity depth, excess PDMS as insulator, microfluidic channel width, and microfluidic channel length. As shown in Figure 2, the structure is indifferent to channel widths and excess PDMS. Optimal parameters were obtained for thicker cavities and longer channel lengths. Thicker excess PDMS leads to additional cost and longer channel lengths lead to more difficulty maintaining a proper hydrodynamic resistance ratio. Cavity and microfluidic channel thickness are limited by SU-8 mold fabrication and PDMS soft lithography to $400\text{ }\mu\text{m}$. There is no optimized value for the post dimension and it can be selected to meet the fabrication method's requirements such as photoresist's maximum deliverable aspect ratio. Distances between the posts are more important than the posts themselves, since they decide the hydraulic resistance in the cross-flow direction. This resistance is directly proportional to the maximum allowable liquid backpressure. Therefore, the void dimension can be selected to tune the maximum achievable velocity of liquid in the sample channel.

With the optimal parameters determined by simulations for fluid channel thickness, fluid channel width, length of fluid channel, and excess PDMS, we select a good system design for the liquid repellent structure and experimentally verify its stability and capability. In order to predict the maximum pressure flow that can be contained in the central channel, we use a similar method as in Ref. 11 except, in our case, the material in the microfluidic channel is PDMS

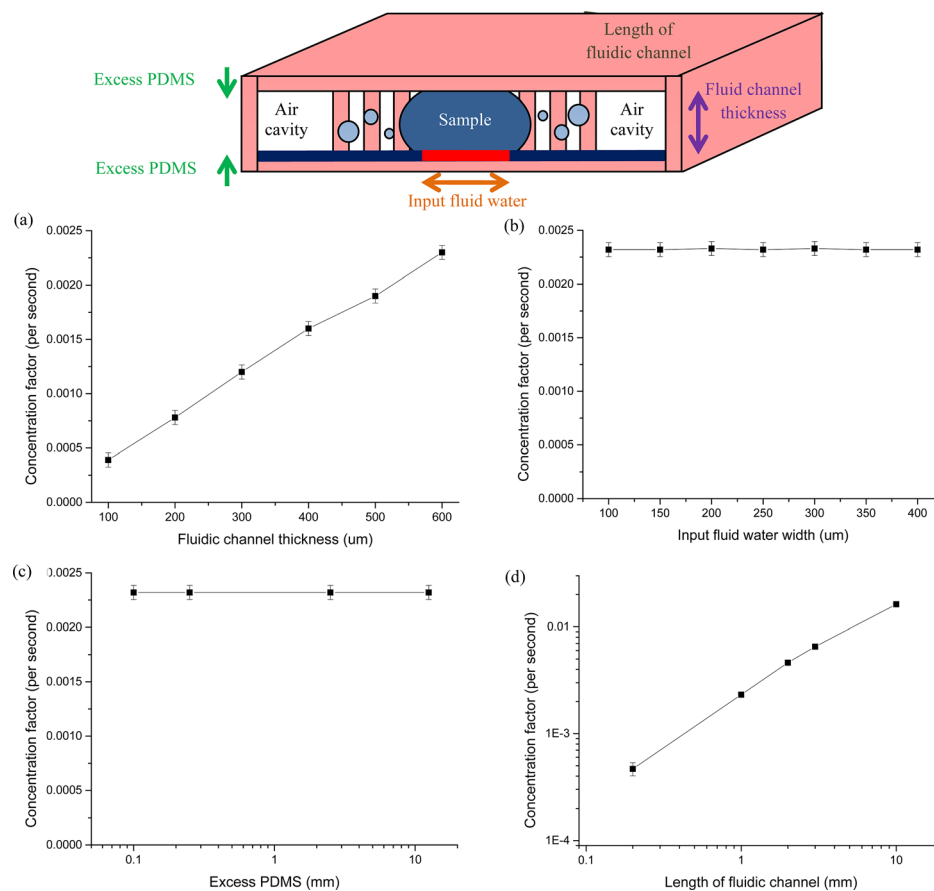


FIG. 2. Optimizing parameters on the liquid repellent structure on a chip. Four parameters were optimized in COMSOL simulations: (a) fluidic channel thickness, (b) input fluidic water width, (c) excess PDMS, and (d) length of fluidic channels. Thicker fluidic channels achieve higher total output, in an almost linear manner. However, thicker fluidic channels are difficult to fabricate as photolithography is generally limited to a 5 : 1 height to width ratio. There is indifference to the water width and excess PDMS thickness. Excess PDMS leads to higher material cost. Finally, longer fluid channel lengths are preferred to shorter ones. Shorter lengths require more precise fluidic flow rates in experiments, otherwise much of the energy is lost in the waste stream. Simulation error bars are due to meshing sensitivity.

rather than silicon. Manipulating the height of the water tank allows us to modify the inlet pressure. We take images of the radius of curvature of the water-air interface at the sample microfluidic channel, as shown in Figure 3. The radius of curvature at the interface is determined by the Laplace-Young equation

$$\Delta P = \gamma \left(\frac{1}{R_x} + \frac{1}{R_y} \right),$$

where γ is surface tension, R_x and R_y are the radii of curvature, and ΔP is the pressure difference between liquid and vapor phase. From the images, we obtain R_x . We can infer R_y from R_x . At a water tank height of 0 mm, the radii of curvature R_x and R_y are ∞ since the pressure inside and outside the water is the same. As the water tank is raised in height, the radii of curvature decrease since the pressure inside the water is higher than in the ambient air. When the water tank is increased to a maximum of 80 mm, the radius of curvature is $R_x < 40 \mu\text{m}$ and the sample enters into the liquid repellent structure.

Second, we calculate the fluidic resistance of the liquid repellent structure. The hydraulic resistance⁴⁴ is determined by

$$R \approx \frac{12 \mu l}{wh^3(1 - 0.630h/w)},$$

for a microfluidic channel with viscosity μ , height h , width w , and length L , where $h < w$. When $w < h$, one can switch the two variables. We assume a fixed fluid viscosity μ and height $h = 400 \mu\text{m}$ for all structures. The two variables are width w and length L . We assume that the fluid must travel from the inlet of the sample microfluidic channel to the outlet of the sample microfluidic channel without any connections between the sample microfluidic channel and the liquid repellent structure.

An equivalent fluidic resistance circuit would be many cross-sections in series consisting of the sample microfluidic channel with width $w = 800 \mu\text{m}$ and length $L = 100 \mu\text{m}$ along with a

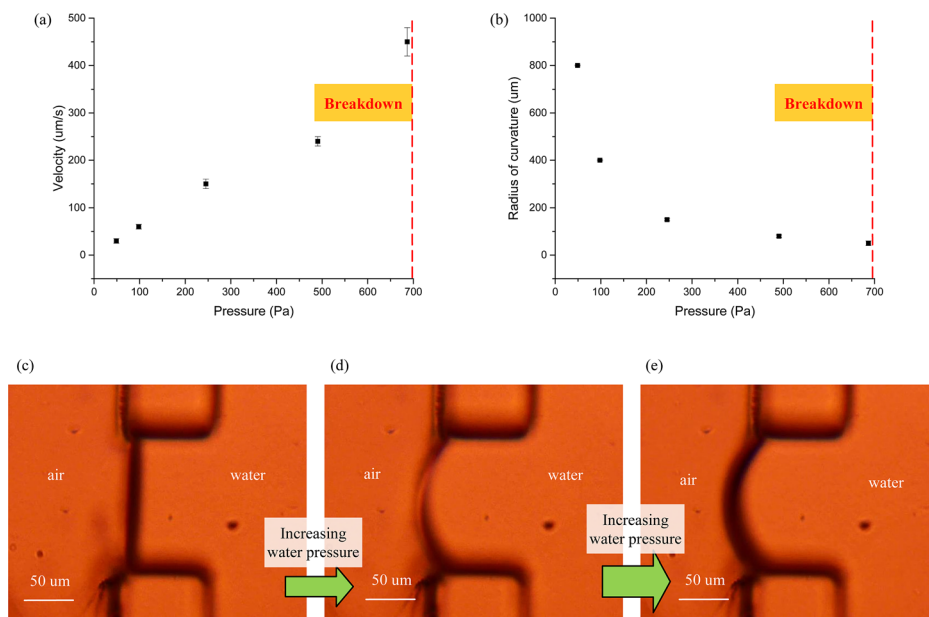


FIG. 3. Graphs (a) and (b) and images (c)–(e) of water velocity and radius of curvature at the water-air interface as the water tank is changed in height experimentally. As the height is increased, the fluid flow velocity increases and the radii of curvature decrease. At some height, the liquid repellent structure does not prevent liquid water from entering into it, a condition we term breakdown. We note that breakdown occurs at 80 mm of height for the water tank. Stable fluid flow is achieved for fluid velocity of $550 \mu\text{m/s}$ and a radius of curvature at $R_x \sim 40 \mu\text{m}$. This is equivalent to $0.2 \mu\text{l/s}$ for the $1 \text{ cm} \times 8 \text{ mm}$ chip or 0.8 ml/h per 1 cm^2 .

side channel with width $w = 100 \mu\text{m}$ and length $L = 500 \mu\text{m}$, connecting from and to the microfluidic channel through the openings in the liquid repellent structure.

Therefore, the fluidic resistance of each parallel small structure is more than 2 orders of magnitude larger than the central fluidic channel. As such, one can expect to have about 100 small openings before the side openings have equivalent fluidic resistance to the sample microfluidic channel. If the openings are $100 \mu\text{m}$ wide, the sample microfluidic channel can be 1 cm long.

With these two parameters: a 75 mm high water tank and a 1 cm long sample microfluidic channel, we know the water pressure and hydrodynamic resistance. The fluidic flow rate is determined by

$$\Delta P = R \times Q,$$

where Q is the volumetric flow rate in the channel and R is the hydrodynamic resistance. Experimentally, the maximum average fluidic velocity is $550 \mu\text{m/s}$ at a radius of curvature at $40 \mu\text{m}$. This is equivalent to $0.2 \mu\text{l/s}$ for $1 \text{ cm} \times 8 \text{ mm}$ chip or 0.8 ml/h per 1 cm^2 .

With these additional calculations, the most practical design was chosen with depth at $400 \mu\text{m}$, 1 cm long microfluidic channel and air cavity, and 2–10 mm total PDMS thickness. In the experiments, we characterized the liquid repellent structure by resolving the following questions: (1) Does the structure keep the liquid separated from the vapour, and (2) How good is the structure at concentrating samples?

EXPERIMENTAL RESULTS

The liquid repellent structure on a chip is very adept at separating vapour and corresponding condensate from the sample in the microfluidic channel. To use the liquid repellent structure to concentrate samples, we modified the input sample temperature while keeping the chip cool. The chip was kept continuously at 20°C ; the body of water in the sample microfluidic channel was pre-heated. Figure 4 shows the results with $50 \mu\text{g/ml}$ Rhodamine 6G (Sigma Aldrich) contaminated water heated to 50°C , visualized with a 50 mW/cm^2 , 514 nm Argon ion laser. Rhodamine 6G containing contaminated water is flowing through the sample microfluidic

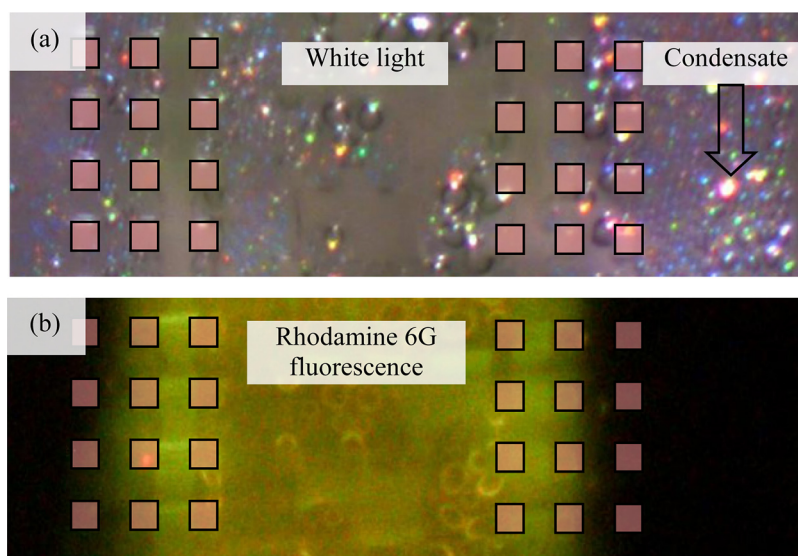


FIG. 4. Experiment of fluorescence concentration using the liquid repellent structure on a chip with Rhodamine 6G contaminated water. A diagram of the liquid repellent structure is overlaid on the images (a) and (b). The Rhodamine 6G is visualized using a 514 nm Argon laser. Rhodamine 6G containing contaminated water, pre-heated to 50°C , is flowing through the sample microfluidic channel. The liquid repellent structure separates the Rhodamine 6G contaminated water from the air cavity. Over time, condensate forms inside the air cavity, which we can see from the light scattering. There is clear separation of the Rhodamine 6G between the air cavity and sample channel.

channel. The liquid repellent structure separates the Rhodamine 6G contaminated water from the air cavity. Over time, condensate forms inside the air cavity, which we can see from the light scattering. There is clear separation of the Rhodamine 6G between the air cavity and sample channel as evidenced by the lack of fluorescence response in the region outside the membrane. The vertical stripes in Figure 4(b) are an artefact due to the fluorescence filter.

To measure sample concentration capability with different pre-heating conditions, we measured the distillate output at different input temperatures. The chip was kept continuously at 20 °C; the body of water in the sample microfluidic channel was pre-heated between 30 °C and 80 °C. Due to the temperature difference and continuous flow of the pre-heated sample, continuous distillation occurs. At 30 °C, we experimentally obtain 0.2 ml/h per 1 cm²; at 80 °C, we experimentally obtain 3.6 ml/h per 1 cm². Simulations were performed with the same parameters as the experiment to quantify distillate output. At 30 °C, we simulate a distillate output of 0.3 ml/h per 1 cm²; at 80 °C, we simulate a distillate output of 5.1 ml/h per 1 cm².

A relationship between distillate output and concentration factor can be determined by the following formula:

$$C_{final} = C_{initial} \cdot \frac{V_{initial} + V_{distillate}}{V_{initial} + V_{waste}},$$

where $C_{initial}$ is the initial concentration of particles, C_{final} is the final concentration of particles, $V_{initial}$ is the initial volume inside the microfluidic channel, $V_{distillate}$ is the distillate output, and V_{waste} is the waste output from the central microfluidic channel.

As shown in Figure 5, there is general agreement on the curve although the simulation output is higher than the experimental results. This factor comes about due to additional losses which were not considered in the simulation of the fluidic channels. For example, in actual experiments $V_{waste} \neq 0$ and there is some heated fluid exiting the system in the outlet but in the simulations, we assume that there is no exiting fluid and that $V_{waste} = 0$. Additionally, some energy is lost as the two bodies of water are quite far from each other and some water vapour may condense in the air cavity closer to the liquid repellent structure and farther away from the cavity walls.

We performed an experiment with fluorescent particles, as shown in Figure 6. The contaminated water, pre-heated to 50 °C, contains 10⁷/ml SYTO9 (Invitrogen) labeled *Escherichia coli* K12 JM101 (Bioconcept), 10⁷/ml yellow-green fluorescent 100 nm latex beads (Invitrogen),

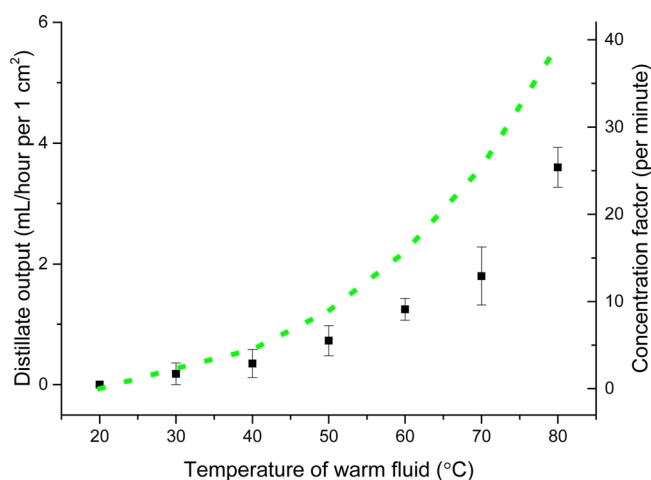


FIG. 5. Comparison of experimental and simulation results of distillate output and concentration factor from the liquid repellent structure on a chip. Experiments were performed with the chip cooled to 20 °C; the body of water in the sample microfluidic channel was heated up to between 30 °C and 80 °C. Simulation results are shown in a dotted green line. Experimental results are plotted with error bars. The simulation output is higher than the experimental results. This factor comes about due to additional losses which were not considered in the simulation of the fluidic channels. For example, in actual experiments, there is additional heated fluid exiting the system as waste which is not all accounted for in the simulations.

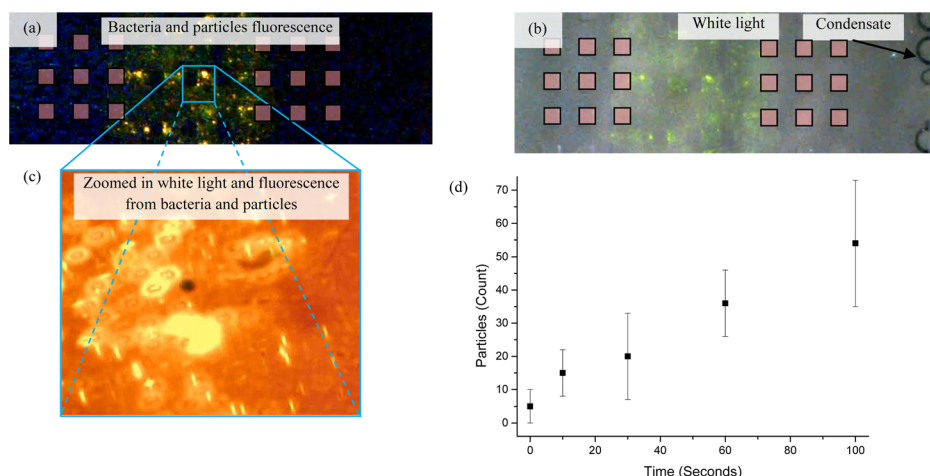


FIG. 6. Experiment of particle concentration using the liquid repellent structure on a chip with SYTO9 labeled *E. coli*, green fluorescent 100 nm and 1 μm particles contaminated water. A diagram of the liquid repellent structure is overlaid on the images (a)–(c). The bacteria and particles are visualized using a 488 nm Argon laser. The contaminated water, pre-heated to 50 $^{\circ}\text{C}$, is inside the sample channel. The liquid repellent structure separates the contaminated water from the air cavity. There is clear separation of the bacteria and particles between the air cavity and sample channel. As we increase the magnification of the imaging system to get a better count of the number of bacteria and particles, most objects appear out-of-focus as the cavity depth is greater than the depth of focus. Therefore, we measure the total particle count by taking several images at different focal depths. We count the number of particles in the field of view as water evaporates over time in (d). There is a 10x concentration of the particles over 100 s, which is in agreement with simulation results.

and $10^7/\text{ml}$ yellow-green fluorescent 1 μm latex beads (Invitrogen). The bacteria and particles are visualized using a 100 mW/cm² 488 nm Argon ion laser. The contaminated water is flowing through the sample channel. As before, the liquid repellent structure separates the contaminated water from the air cavity. The outlet is closed to prevent continuous flow. Over time, the particle concentration increases; the temperature in the sample microfluidic channel decreases until it is in equilibrium with the entire microfluidic chip. We see 10x concentration of the particles over 100 s.

DISCUSSION

Experiments with evaporation-based concentration methods are limited by the ambient environment (i.e., humidity, room temperature, etc.).¹⁶ Control of the evaporating surface, which determines the amount of liquid evaporating into vapour, and the heat sink, which removes the excess vapour, requires precise control of both the evaporating surface area and the thermal gradient. Although both concepts were demonstrated external to the microfluidic chip,^{17,18,24} we demonstrate the capability to control the two factors within the microfluidic chip to perform sample concentration. Experiments with open surface microchannel grooves 25 provide a very similar basis to compare against our results. With the hot body of water at 20 $^{\circ}\text{C}$, air velocity at 0.15 ms⁻¹ and relative humidity at 50%, they are able to obtain 2% increase in particle concentration per 1 s with a 125 μm wide and 80 μm deep channel. 50% relative humidity at 20 $^{\circ}\text{C}$ is equivalent to saturated humidity at about 9 $^{\circ}\text{C}$. If we interpolate the data from our experiments, we are capable of experimentally obtaining 2% increase in sample concentration per 1 s by having the hot body of water at 28 $^{\circ}\text{C}$ and the heat sink at 20 $^{\circ}\text{C}$. If one looks at the saturated vapour pressures for these two temperatures, the change in vapour pressure is very similar. Therefore, we obtain very similar results for sample concentration with an evaporation based microfluidic device in a much smaller footprint.

CONCLUSION

We have demonstrated using a liquid repellent structure to perform both distillation and evaporation based sample concentration in-plane inside a microfluidic chip. We demonstrate

3.6 ml/h per 1 cm² distillate output using two bodies of water at 20 °C and 80 °C. Using the same structure, we demonstrate 10x concentration of fluorescent particles over 100 s. We anticipate that the proposed microfluidic structure will enable novel applications in communicating microchannels within integrated lab-on-a-chip systems. The approach is lightweight, low cost, and of low complexity.

ACKNOWLEDGMENTS

Part of the research was performed under the financial support of the Nano-Tera initiative for the Solar Hydrogen Integrated Nano Electrolyzer (SHINE) project's Grant No. 20NA21-145936. The authors would like to thank Wuzhou Song, Marcin Zielinski, Ye Pu, Xin Yang, Gregoire Laporte, and Miguel Modestino for their helpful discussions.

- ¹P. Neuzil, S. Giselbrecht, K. Lange, T. J. Huang, and A. Manz, *Nat. Rev. Drug Discovery* **11**, 620–632 (2012).
- ²A. C. Glavan, R. V. Martinez, E. J. Maxwell, A. B. Subramaniam, R. M. D. Nunes, S. Soh, and G. M. Whitesides, *Lab Chip* **13**, 2922–2930 (2013).
- ³J. H. So and M. D. Dickey, *Lab Chip* **11**, 905–911 (2011).
- ⁴B. Mustin and B. Stoeber, *Lab Chip* **12**, 4702–4708 (2012).
- ⁵A. J. Mach, J. H. Kim, A. Arshi, S. C. Hur, and D. Di Carlo, *Lab Chip* **11**, 2827–2834 (2011).
- ⁶D. Choudhury, X. Mo, C. Ilescu, L. L. Tan, W. H. Ton, and H. Yu, *Biomicrofluidics* **5**, 022203 (2011).
- ⁷R. Martinez-Duarte, *Electrophoresis* **33**, 3110–3132 (2012).
- ⁸M. Hitzbleck, L. Avrain, V. Smeken, R. D. Lovchik, P. Mertens, and E. Delamarche, *Lab Chip* **12**, 1972–1978 (2012).
- ⁹K. N. Knust, D. Hlushkou, R. K. Anand, U. Tallarek, and R. M. Crooks, *Angew. Chem., Int. Ed.* **52**, 8107–8110 (2013).
- ¹⁰E. Berthier, J. Warrick, H. Yu, and D. J. Beebe, *Lab Chip* **8**, 860–864 (2008).
- ¹¹K. F. Lam, E. Cao, E. Sorensen, and A. Gavrilidis, *Lab Chip* **11**, 1311–1317 (2011).
- ¹²K. F. Lam, E. Sorensen, and A. Gavrilidis, *Chem. Eng. Res. Des.* **91**, 1941–1953 (2013).
- ¹³K. F. Jensen, *Chem. Eng. Sci.* **56**, 293–303 (2001).
- ¹⁴V. Hessel, P. Angeli, A. Gavrilidis, and H. Lowe, *Ind. Eng. Chem. Res.* **44**, 9750–9769 (2005).
- ¹⁵A. Gunther and K. F. Jensen, *Lab Chip* **6**, 1487–1503 (2006).
- ¹⁶G. M. Walker and D. J. Beebe, *Lab Chip* **2**, 57–61 (2002).
- ¹⁷C. S. Effenhauser, H. Harttig, and P. Kramer, *Biomed. Microdevices* **4**, 27–32 (2002).
- ¹⁸M. Zimmermann, S. Bentley, H. Schmid, P. Hunziker, and E. Delamarche, *Lab Chip* **5**, 1355–1359 (2005).
- ¹⁹Y. H. Choi, S. S. Lee, and K. H. Chung, *BioChip J.* **4**, 63–69 (2010).
- ²⁰J. Y. Zhang, J. Do, W. R. Premasiri, L. D. Ziegler, and C. M. Klapperich, *Lab Chip* **10**, 3265–3270 (2010).
- ²¹Z. R. Xu, C. H. Zhong, Y. X. Guan, X. W. Chen, J. H. Wang, and Z. L. Fang, *Lab Chip* **8**, 1658–1663 (2008).
- ²²J. Y. Zhang, M. Mahalanabis, L. Liu, J. Chang, N. R. Pollock, and C. M. Klapperich, *Diagnostics* **3**, 155–169 (2013).
- ²³N. S. Lynn and D. S. Dandy, *Lab Chip* **9**, 3422–3429 (2009).
- ²⁴X. Casadevall i Solvas, V. Turek, T. Prodromakis, and J. B. Edel, *Lab Chip* **12**, 4049–4054 (2012).
- ²⁵S. Kachel, Y. Zhou, P. Scharfer, C. Vrancic, W. Petrich, and W. Schabel, *Lab Chip* **14**, 771–778 (2014).
- ²⁶C. C. Wong, Y. Liu, K. Y. Wang, and A. R. A. Rhaman, *Lab Chip* **13**, 3663–3667 (2013).
- ²⁷F. de Angelis, F. Gentile, F. Mecarini, G. Das, M. Moretti, P. Candeloro, M. L. Coluccio, G. Cojoc, A. Accardo, C. Liberale, R. P. Zaccaria, G. Perozziello, L. Tirinato, A. Toma, G. Cuda, R. Cingolani, and E. di Fabrizio, *Nat. Photonics* **5**, 682–687 (2011).
- ²⁸N. S. Lynn, C. S. Henry, and D. S. Dandy, *Lab Chip* **9**, 1780–1788 (2009).
- ²⁹D. Erickson, D. Sinton, and D. Psaltis, *Nat. Photonics* **5**, 583–590 (2011).
- ³⁰K. S. Elvira, X. Casadevall i Solvas, R. C. R. Wootton, and A. J. deMello, *Nat. Chem.* **5**, 905–915 (2013).
- ³¹J. Haber, M. N. Kashid, A. Renken, and L. Kiwi Minsker, *Ind. Eng. Chem. Res.* **51**, 1474–1489 (2012).
- ³²Y. Zhang, in *International Symposium on Photonics and Optoelectronics* (2012).
- ³³Y. F. Chen, L. Jiang, M. Mancuso, A. Jain, V. Oncescu, and D. Erickson, *Nanoscale* **4**, 4839–4857 (2012).
- ³⁴J. Melin, W. van der Wijngaart, and G. Stemme, *Lab Chip* **5**, 682–686 (2005).
- ³⁵D. D. Meng and C. J. Kim, *Lab Chip* **8**, 958–968 (2008).
- ³⁶A. M. Skelley and J. Voldman, *Lab Chip* **8**, 1733–1737 (2008).
- ³⁷W. Zheng, Z. Wang, W. Zhang, and X. Jiang, *Lab Chip* **10**, 2906–2910 (2010).
- ³⁸C. Liu, J. A. Thompson, and H. H. Bau, *Lab Chip* **11**, 1688–1693 (2011).
- ³⁹S. Harrer, S. Ahmed, A. Afzali-Ardakani, B. Luan, P. S. Waggoner, X. Shao, H. Peng, D. L. Goldfarb, G. J. Martyna, S. M. Rossenagel, L. Deligianni, and G. Stolovitzky, *Langmuir* **26**, 19191–19198 (2010).
- ⁴⁰C. Lochoovsky, S. Yasotharan, and A. Gunther, *Lab Chip* **12**, 595–601 (2012).
- ⁴¹J. M. Karlsson, M. Gazin, S. Laakso, T. Haraldsson, S. Malhotra-Kumar, M. Maki, H. Goossens, and W. van der Wijngaart, *Lab Chip* **13**, 4366–4373 (2013).
- ⁴²A. Oskoei, M. Abolhasani, and A. Gunther, *Lab Chip* **13**, 2519–2527 (2013).
- ⁴³M. S. Plesset, *J. Chem. Phys.* **20**, 790–793 (1952).
- ⁴⁴H. Bruss, *Theoretical Microfluidics* (Oxford University Press, 2008).